RSC Advances

ROYAL SOCIETY OF CHEMISTRY

www.rsc.org/advances

Adsorption behavior and removal mechanism of arsenic on graphene modified by iron-manganese binary oxide ($FeMnO_x$/RGO) from aqueous solutions

Jin Zhu[a], Zimo Lou[a], Yu Liu[a], Ruiqi Fu[a], Shams Ali Baig[a,b], Xinhua Xu[a,*]

[a]Department of Environmental Engineering, College of Environmental and Resource Sciences, Zhejiang University, Hangzhou 310058, People's Republic of China

[b]Department of Environmental Sciences, COMSATS Institute of Information Technology (CIIT), Abbottabad 22060, Pakistan

[*]Corresponding author: Tel: +86-571-88982031; Fax: +86-571-88982031.
E-mail address: xuxinhua@zju.edu.cn

Abstract

Iron-manganese binary oxide ($FeMnO_x$) is considered highly effective for arsenic adsorption, however, the agglomeration effect hindered its practical application. In this study, graphene has been used as a supporting matrix to disperse $FeMnO_x$ due to its huge specific surface area, and the synthesized novel composite adsorbent ($FeMnO_x$/RGO) was employed for arsenic removal. Results demonstrated that $FeMnO_x$/RGO (mass ratio of $FeMnO_x$ to $FeMnO_x$/RGO nanocomposites is 45%) has larger specific surface area (411 m^2 g^{-1}) in comparison with bare $FeMnO_x$, and showed 10.16 mg As g^{-1} $FeMnO_x$ and 11.49 mg As g^{-1} $FeMnO_x$ adsorption capacities for As(III) and As(V), respectively, with 1 mg L^{-1} initial concentration. Increased in the initial concentration to 7 mg L^{-1}, the adsorption capacities of As(III) and As(V) reached to 47.05 mg As g^{-1} $FeMnO_x$ and 49.01 mg As g^{-1} $FeMnO_x$, respectively. The removal process perfectly obeys pseudo second-order kinetic model for both As(III) and As(V). And PO_4^{3-} was found to strongly inhibit arsenic adsorption. Furthermore, adsorption tests and characterization analyses confirmed that MnO_2 played a key role on the oxidation of As(III), while iron(III) oxide was found crucial to As(V) removal. Electrostatic interaction and surface complexation mechanisms involved in the adsorption. These findings suggested that the adsorbent could be used in real arsenic-contaminated water treatment.

Keywords: Graphene; Fe-Mn binary oxide; Arsenic removal; Mechanism.

1. Introduction

Arsenic is one of the most toxic and carcinogenic chemical elements and its contamination in natural waters has become a worldwide problem[1]. Long-term exposure to drinking water containing arsenic can give rise to cancers of skin, lungs, liver, kidney and bladder, as well as hypertension and cardiovascular disease [2]. To minimize associated health risks, the World Health Organization (WHO) and US Environmental Protection Agency (USEPA) have set a more stringent standard value for arsenic in drinking water from 0.05 to 0.01 mg L^{-1} in 1990s[3, 4]. Inorganic forms of arsenic mainly exist in natural water environments. The inorganic forms, arsenite (As(III)) and arsenate (As(V)), are thought to be more toxic than the organic arsenic species. In general, As(III) exists in groundwater, while As(V) is dominate in surface water bodies[5-7]. In addition, As(III) is more soluble and toxic than As(V) and it is less efficient to be removed because of its mobility in water and low affinity towards adsorbents [8].

In recent years, due to growing concerns of arsenic contamination in water bodies, numerous methods have been developed and adsorption is considered to be one of the most promising technologies due to its simple operation and low cost[9, 10]. Nowadays, a variety of materials have been used as adsorbents for arsenic removal, such as granular ferric hydroxide[11], Fe-Mn binary oxide[12], activated carbon[13], alumina[14], and so on. Among these materials, Fe-Mn binary oxide has been widely studied for arsenic remediation[15, 16]. The combination can take full advantages of the

73 excellent oxidation potential of manganese dioxide for As(III) and the superior
74 adsorption ability of iron(III) oxide for arsenic removal from aqueous solutions.
75 However, bare Fe-Mn binary oxide exhibits high tendency to agglomerate, so that the
76 adsorption properties will be weakened, limiting its full-scale application. In order to
77 overcome this problem, providing a carrier such as multiwalled carbon nanotubes[17],
78 activated carbon [18], graphene[19], and wheat straw[20] to disperse particles of Fe-Mn
79 binary oxide seems to be a better alternative for enhanced arsenic removal.

80 Graphene, a two-dimensional structure of sp^2-bonded carbon with only one-atom
81 thick, possesses huge theoretical specific surface area (2630 m^2 g^{-1}), good electrical
82 conductivity, high thermal conductivity and intrinsic mobility[21]. Compared to other
83 carbon-based materials, such as activated carbon and multiwalled carbon nanotubes,
84 graphene sheets have higher specific surface area, which provides more active
85 adsorption sites for Fe-Mn binary oxide loading. Furthermore, their superior electrical
86 conductivity can promote electron transport between Fe-Mn binary oxide and targeted
87 contaminants in the adsorption process[22]. Therefore, utilizing graphene as a supporter
88 for adsorbents' synthesis attracts its wide application in pollutant remediation
89 measures.

90 In our previous study, honeycomb briquette cinders (HBC) were used as a carrier
91 to coat with Fe_3O_4 and MnO_2 for arsenic removal, certifying that Fe_3O_4 and MnO_2
92 had good affinity to arsenic[23]. Nanoscale zero-valent iron (nZVI) assembled on
93 magnetic Fe_3O_4/graphene for Cr(VI) removal was studied to confirm that graphene

was an excellent supporter to disperse and stabilize nZVI particles[22]. Therefore, in this study, graphene modified by iron-manganese binary oxide ($FeMnO_x$/RGO) was synthesized and to reduce the associated costs, graphene was derived from exfoliation of graphite oxide followed by reduction. Characterization techniques including TEM, XRD, FTIR, BET and XPS were applied to characterize the adsorbent composites. Effect of loading ratios of Fe-Mn binary oxide was studied to explain the role of graphene and examine the removal efficiency of As(III) and As(V). Adsorption isotherms and adsorption kinetics were performed to explore the adsorbent properties. Effects of competing ions on As(III)/ As(V) were also investigated. And effects of initial pH, various molar ratios of iron to manganese on graphene were carried out to identify the possible removal mechanism.

2. Materials and methods

2.1. Materials

Chemicals used in this study were of analytical grade except hydrochloric acid (GR). Graphite powder and hydrazine hydrate were purchased from Aladdin Reagent Database Inc., China. Potassium permanganate ($KMnO_4$), sulfuric acid (H_2SO_4) 98%, sodium nitrate, hydrogen peroxide (H_2O_2) 30%, ammonia, ferrous sulfate heptahydrate ($FeSO_4 \cdot 7H_2O$), manganese (II) sulfate monohydrate ($MnSO_4 \cdot H_2O$), sodium hydroxide and sodium hypochlorite were purchased from Sinopharm Chemical Reagent Co., Ltd, China.

As(III) and As(V) stock solutions (1000 mg L^{-1}) were prepared by dissolving

appropriate amount of sodium arsenite ($NaAsO_2$) and sodium arsenate dodecahydrate ($Na_3AsO_4 \cdot 12H_2O$) in purified water, respectively. Thiourea, L-ascorbic acid and potassium borohydride were utilized for arsenic detection.

2.2. Preparation of RGO

Graphite oxide was synthesized through a modified Hummer's method[24]. In brief, 120 mL concentrated sulfuric acid was added into a 500 mL three-neck flask and then the flask was put in water bath containing ice bags with continuous stirring at 200 rpm. At 10 ^{o}C, 5.0 g graphite powder, 2.5 g $NaNO_3$ and 15 g $KMnO_4$ were added separately into the flask. After removing ice bags, the suspension was stirred overnight until its color turned into light gray and the mixture became pasty. Then 150 mL water was slowly added into the mixture to dilute the paste and the reaction temperature was heated to 98 ^{o}C for 2 h. Later on, 50 mL H_2O_2 was added and the mixture continued stirring for another 30 min. The product was washed by 5% HCl, ethanol and deionized water, and then dried in vacuum oven at 60 ^{o}C.

Approximately 1.6 g synthesized graphitic oxide was re-dispersed in 800 mL deionized water and exfoliated by ultrasonication for 1.5 h to obtain graphene oxide. Subsequently, 19.2 mL hydrazine solution (50%) and 22.72 mL ammonia solution (25%) were added to reduce graphene oxide into graphene. The reaction was held for 3 h at 98 ^{o}C and then the mixture was centrifuged, rinsed by deionized water and filtered through a 0.45 μm filter membrane. Finally, the product was dried in vacuum at 60 ^{o}C and stored for subsequent experiments.

136 *2.3. Preparation of $FeMnO_x$/RGO*

137 The fabrication of $FeMnO_x$/RGO was followed by a co-precipitation
138 process[16]with some modifications. Firstly, 0.2 g graphene was dispersed in deionized
139 water under ultrasonic wave for 1.5 h to obtain uniform black suspension, followed by
140 the addition of desired amounts of $KMnO_4$ and $FeSO_4 \cdot 7H_2O$ under vigorous stirring.
141 At the same time, 5 M NaOH was added to adjust pH value to 7-8. Then the mixture
142 was continuously stirred for 2 h at 60 ^oC and aged at room temperature for 12 h.
143 Finally, the material was separated, rinsed and dried for further use.

144 When the molar ratio of Fe:Mn was 3:1, different mass ratios of generated
145 Fe-Mn binary oxide on graphene to the whole nanocomposites were prepared, mass
146 ratios of $FeMnO_x$ to $FeMnO_x$/RGO nanocomposites are 14%, 45% and 76.5%,
147 respectively. For instance, to obtain $FeMnO_x$/RGO with mass ratio of $FeMnO_x$ 45%,
148 0.079 g $KMnO_4$ and 0.4170 g $FeSO_4 \cdot 7H_2O$ were added for reaction. Fe-Mn binary
149 oxide ($FeMnO_x$) was also synthesized for comparison using the method employed by
150 Zhang et al.[16].

151 Using $FeMnO_x$/RGO (nFe:nMn=3:1, mass ratio of $FeMnO_x$ to $FeMnO_x$/RGO
152 nanocomposites is 45%) as a standard, different molar ratios of Fe:Mn were prepared.
153 As the amount of $FeSO_4 \cdot 7H_2O$ was 0.4170 g, change the dosage of $KMnO_4$ to make
154 nFe:nMn=3:0.5,3:2 and 3:4, respectively. In contrast, while 0.079g $KMnO_4$ was added,
155 the dosage of $FeSO_4 \cdot 7H_2O$ was changed to make nFe:nMn=0.5:1, 1:1 and 4:1,
156 respectively.

In order to better understand the removal mechanism, FeO_x/RGO (0.2 g RGO, 0.4170 g $FeSO_4 \cdot 7H_2O$) and MnO_x/RGO (0.2 g RGO, 0.0507 g $MnSO_4 \cdot H_2O$, 0.0316 g $KMnO_4$) were synthesized to compare with $FeMnO_x$/RGO. Theoretically, the amount of obtained MnO_2 in MnO_x/RGO was the same as that in $FeMnO_x$/RGO.

2.4. Characterization and analytical methods

TEM (JEM-1230, JEOL, Japan) analyses were conducted to know the morphological structures of bare graphene, $FeMnO_x$ and $FeMnO_x$/RGO. XRD analysis (X'pert PRO analytical B.V., Netherlands) of the samples was performed in 2θ scale. The specific surface area and porosity data were analyzed by a BET analyzer (ASIC-2, USA). Functional groups and valence states of elements were investigated by FTIR (IRaffinity-1, SHIMADZU, Japan) and XPS (Kratos Axis Ultra DLD, SHIMADZU, Japan), respectively.

PZC determination of RGO, $FeMnO_x$ and $FeMnO_x$/RGO was obtained using a Zeta Meter 3.0 (Zetasizer3000HSA, UK). 0.01g adsorbent was added into five 100 mL conical flasks with 50 mL deionized water, respectively. And the mixture was under ultrasonic wave for 20 min to obtain uniform suspension. Then adjust pH values to 2, 4, 6, 8 and 10, respectively. So zeta potentials under different pH values could be measured.

Total arsenic concentration was measured by an AFS-230E atomic fluorescence spectrophotometer (Beijing Kechuang Haiguang Instrument Company, China). Solution of 5% L-ascorbic acid and 5% thiourea was employed to act as a reducing

178 reagent.

179 *2.5. Batch adsorption experiments*

180 Adsorption isotherms were conducted at temperature 25 ^{o}C and pH 7.0 ± 0.1.
181 Adsorbent dose of 0.01 g was added into 50 mL 0.2, 0.6, 1.0, 3.0, 5.0, 7.0 mg L^{-1}
182 As(III) or As(V) solution, respectively. And then the suspension was mixed by a
183 rotary shaker (SUKUN, SKY-110WX, Shanghai, China) at 180 rpm. Samples were
184 taken out using syringe and filtered through a 0.45 μm filter membrane after 24 h for
185 arsenic detection.

186 Kinetic studies were examined by batch experiments at different time intervals
187 from 5 min to 24 h with 1 mg L^{-1} initial arsenic concentration and 0.2 g L^{-1} adsorbent
188 dose. Effects of competing ions (SO_4^{2-}、HCO_3^-、PO_4^{3-}) on arsenic removal were
189 investigated by varying the ionic concentration ranges (0-10 mM). Effect of initial pH
190 on arsenic removal was tested by changing pH values from 3-11. Other conditions
191 were kept the same as for isotherm experiments. All batch adsorption experiments
192 were performed in triplicate, and the average values were reported.

193 *2.6. Adsorbent desorption and regeneration*

194 In order to study the regeneration potential of the sorbent, five consecutive
195 adsorption-regeneration cycles were performed. 0.01 g adsorbent was added into 50
196 mL 100 μg L^{-1} As(III) or As(V) solution for adsorption and then 0.1 M NaOH + 0.1 M
197 NaClO was used as the regenerant.

198 ## 3. Results and discussion

199 *3.1. Characterization of adsorbents*

200 TEM images reveal the morphological structures of RGO, $FeMnO_x$ as well as
201 $FeMnO_x$/RGO with different loading ratios of Fe-Mn binary oxide. The folding nature
202 of graphene sheets was clearly visible in Fig. 1a. It can be observed that graphene
203 possesses crumpled and silk wave-like structure, confirming that the reduced graphite
204 oxide was successfully formed. Fig. 1b shows that particles of iron-manganese binary
205 oxide agglomerated severely with each other, which could result in a dramatic decline
206 in the functions of Fe-Mn binary oxide for arsenic removal. Irregular shapes of Fe-Mn
207 binary oxide particles were found to attach tightly on graphene sheets (Fig.1c-e). They
208 were well dispersed on the surface of RGO, however, the average diameter increased
209 with the increase of $FeMnO_x$ loading ratios. It can be clearly seen that the particle size
210 of Fe-Mn binary oxide assembled on graphene was less than 10 nm when the mass
211 ratio of $FeMnO_x$ to $FeMnO_x$/RGO nanocomposites was 14%. However, the Fe-Mn
212 binary oxide diameter was found to be 20-50 nm when the mass ratio was 45%. As
213 the loading ratio achieved 76.5%, the average diameter (50-80 nm) was further
214 increased, indicating the occurrence of a slight aggregation effect. Therefore,
215 $FeMnO_x$/RGO with appropriate loading ratios of Fe-Mn binary oxide could be more
216 conductive to arsenic adsorption.

217 According to Table S1, the specific surface areas of RGO, Fe-Mn binary
218 oxidewere measured to be 548 m^2 g^{-1} and 360 m^2 g^{-1}, respectively. In the presence of

graphene possessing higher surface area, the specific surface area of $FeMnO_x$/RGO became larger compared to the unsupported Fe-Mn binary oxide[25]. And when the mass ratios of $FeMnO_x$ to $FeMnO_x$/RGO increased, the surface area decreased because more active sites were occupied by $FeMnO_x$ particles. The BET surface area of $FeMnO_x$/RGO was 411 m^2 g^{-1}, which was obtained from the nitrogen adsorption-desorption isotherms in Figure S1. A typical type-IV curve was observed, which was characteristic for mesoporous materials[26]. Further, the isotherms exhibited a H2 hysteresis loop at a relative pressure from 0.4, implying that the adsorbent was a porous structure[27, 28]. According to Barrett-Joyner-Halenda (BJH) equation, the mean pore size in $FeMnO_x$/RGO was 5.62 nm and the total pore volume was measured to be 0.59 cm^3 g^{-1} (Table S1), which was similar to the result of graphene, indicating that no major effect on porous structure occurred during the loading process, and bare $FeMnO_x$ also had a porous structure and high surface area, which was effective to arsenic adsorption.

Fig. S2 presents XRD patterns of RGO, $FeMnO_x$ and $FeMnO_x$/RGO. As shown in Fig. S2a, two typical peaks at 2θ = 25.0°, 44.0° corresponded to (002) and (100) reflections of graphene sheets[22]. In Fig. S2b, no obvious crystalline peak emerged, indicating that iron oxide and manganese oxide mainly existed in an amorphous form. The results were consistent with studies reported by Zhang et al.[12], and the formation of crystalline iron(III) oxides and manganese oxide could be blocked by their coexistences during the preparation process. After combining graphene with Fe-Mn

240 binary oxide, reductions in the diffraction peaks of graphene were noticed (Fig. S2c),
241 which might be attributed to more disordered stacking and less agglomeration of
242 graphene in the synthesized composite[29].

243 FTIR spectrums of RGO, $FeMnO_x$ and $FeMnO_x$/RGO are shown in Fig. 2. And
244 the magnification of relevant peaks from 400 to 1900 cm^{-1} wavenumber is given in
245 Figure S3. Peak at λ value of 3410 cm^{-1} was assigned to O-H stretching vibrations in
246 water molecules[30]. The band appeared at 1625 cm^{-1} could be attributed to the
247 hydroxyl deformation in water molecules indicating the presence of physisorbed
248 water on the adsorbents[31]. In the spectra of RGO, a broad band at 1040 cm^{-1} was the
249 typical characteristic of C-O stretching vibration, and the presence of a weak band at
250 1560 cm^{-1} was assigned to the skeletal vibration of the unoxidized graphite[30],
251 demonstrating that most part of graphene oxide has been reduced to RGO. The
252 absorption band at 450 cm^{-1} corresponding to Mn-O vibration[19] revealed the existence
253 of residual $KMnO_4$. Three small peaks appeared at 1125 cm^{-1}, 1046 cm^{-1} and 976 cm^{-1}
254 in $FeMnO_x$ and $FeMnO_x$/RGO were assigned to the bending vibrations of Fe-OH[32],
255 indicating the successful formation of iron oxide. The band at 450 cm^{-1} corresponding
256 to Mn-O vibration strengthened after coating with Fe-Mn binary oxide on graphene[19],
257 which revealed that particles of manganese oxide were integrated onto the basal plane
258 of graphene.

259 *3.2. Effect of loading ratios of Fe-Mn binary oxide*

260 Fig. 3 compares the effect of different mass ratios of Fe-Mn binary oxide to

261 $FeMnO_x$/RGO nanocomposites for (a) As(III) and (b) As(V) adsorption. As presented
262 in Fig. 3a, the adsorption capacity of $FeMnO_x$/RGO for As(III) removal improved as
263 the mass ratio of Fe-Mn binary oxide to $FeMnO_x$/RGO increased. However, in Fig. 3b,
264 there was little difference in the removal efficiency of As(V) when the mass ratios
265 were 45% and 76.5%, indicating that higher proportion of Fe-Mn binary oxide might
266 hinder As(V) adsorption on $FeMnO_x$/RGO nanocomposites due to particle
267 aggregation effect. This phenomenon could also be inferred from TEM images in Fig.
268 1. Moreover, Fig. 3 shows that $FeMnO_x$/RGO had lower adsorption ability for both
269 As(III) and As(V) removal as the mass ratio of $FeMnO_x$ was 14%, because the
270 composition of Fe-Mn binary oxide containing in this nanocomposite was also lower.

271 Langmuir and Freundlich isotherm models were employed to describe the data of
272 arsenic adsorption. The Langmuir model[33] and the Freundlich model[34] are expressed
273 as follows:

274 $$\frac{C_e}{q_e} = \frac{1}{bq_m} + \frac{C_e}{q_m} \qquad (1)$$

275 $$\ln q_e = \ln K_F + \frac{1}{n} \ln C_e \qquad (2)$$

276 where q_e and q_m stand for the equilibrium adsorption amount and the maximum
277 adsorption amount of As(III) or As(V) (mg g^{-1}), respectively, C_e is the equilibrium
278 concentration of arsenic (mg L^{-1}), and b is the Langmuir constant, which represents
279 the free energy of adsorption (L mg^{-1}). K_F and n are the Freundlich parameters, which
280 are related to the capacity and intensity of the sorbent, respectively. Generally,
281 adsorption is considered to be favorable when $0.1<1/n<0.5$, whereas it is difficult

adsorbed when $1/n>2$[35].

The fitting data of different kinds of sorbents are listed in Table 1. It can be seen that the Freundlich isotherm matched well with As(III) adsorption on $FeMnO_x$/RGO with various ratios of Fe-Mn binary oxide and the values of n were all between 1 and 10[19], indicating favorable adsorption on the sorbents. In contrast, As(V) adsorption was better described by the Langmuir model.

In order to determine the optimal loading ratios of Fe-Mn binary oxide more persuasively, Table 2 summarized the arsenic adsorption capacity of $FeMnO_x$/RGO with different loading ratios of Fe-Mn binary oxide when the initial arsenic concentration was 7 mg L^{-1}. Meanwhile, RGO and bare Fe-Mn binary oxide were used for comparison. From Table 2, it was obvious that RGO had subtile influence on arsenic removal, which meant that graphene only acted as a favorable carrier to disperse iron and manganese oxides and provided high specific surface area for Fe-Mn binary oxide loading. As can be clearly seen in Table 2, the adsorption capacities of Fe-Mn binary oxide assembled onto RGO with different loading ratios for both As(III) and As(V) removal were much higher than bare Fe-Mn binary oxide. Therefore, using RGO as a template can effectively enhance the adsorption ability of Fe-Mn binary oxide. The possible reason might be that RGO could prevent the particles of Fe-Mn binary oxide from aggregating due to its high specific surface area, so that active adsorption sites increased with the help of graphene, resulting in the enhancement of adsorption capacity.

As shown in Table 2, $FeMnO_x$/RGO owned the maximum equilibrium adsorption capacities for As(III) and As(V), which were found to be 47.05 mg As g^{-1} $FeMnO_x$ and 45.95 mg As g^{-1} $FeMnO_x$. Furthermore, Table 3 compares arsenic adsorption capacity with some adsorbent materials in references, it showed that the synthesized $FeMnO_x$/RGO in our study possessed excellent adsorption capacity for arsenic removal. Thus, $FeMnO_x$/RGO (nFe:nMn=3:1, mass ratio of $FeMnO_x$ to $FeMnO_x$/RGO nanocomposites is 45%) was used for further experiments.

3.3. Sorption kinetics

Effect of contact time on As(III) or As(V) uptake onto the $FeMnO_x$/RGO nanocomposites is shown in Fig. 4. The adsorption process was initially rapid in first 2 h for both As(III) and As(V), after which the adsorption capacity remained slowdown and reached to an equilibrium state within 12 h. As the initial arsenic concentration was 1 mg L^{-1}, the equilibrium adsorption capacities of the adsorbent for As(III) and As(V) were 4.57 mg g^{-1} and 5.17 mg g^{-1}, respectively. Therefore, it was observed that $FeMnO_x$/RGO exhibited faster and greater adsorption ability for As(V) than As(III).

The pseudo-first-order kinetic model[40] and pseudo-second-order kinetic model[41] were used to describe the experimental data. The linear forms are presented as follows:

$$\ln(q_e - q_t) = \ln q_e - k_1 t \qquad (3)$$

$$\frac{t}{q_t} = \frac{1}{k_2 q_e^2} + \frac{1}{q_e} t \qquad (4)$$

where q_e (mg g^{-1}) represents the amount of arsenic adsorbed at the equilibrium time, q_t (mg g^{-1}) is the solid-phase loading of arsenic at time t (min); k_1 and k_2 are the rate constants for the pseudo-first-order model and the pseudo-second-order model, respectively.

The results in Table 4 indicated that the pseudo-second-order model ($R^2 \geq 0.9989$) fitted perfectly with the experimental data for both As(III) and As(V). What's more, the calculated q_e values derived from the pseudo-second-order model were close to the experimental q_e (Table 4). That is to say, the rate-limiting step of arsenic adsorption on $FeMnO_x$/RGO was chemical adsorption between the adsorbent and the adsorbate rather than a mass transfer in solutions[42].

3.4. Effect of competing ions

Figure 5 presents the influence of various competing ions (SO_4^{2-}、HCO_3^-、PO_4^{3-}) on As(III) and As(V) removal by $FeMnO_x$/RGO. It can be seen that SO_4^{2-} at different concentrations affected little on arsenic removal efficiency. Whereas, HCO_3^- and PO_4^{3-} at the studied concentration range showed significant influence on arsenic removal.

HCO_3^- inhibited As(V) adsorption more remarkably than As(III), because As(V) usually exists as anionic species in aqueous solutions[14]. Thus, HCO_3^- and As(V) would compete for the active adsorption sites on the adsorbent to form more stable surface complexes with iron (oxy)hydroxides[43].

As presented in Fig. 5, when the concentration of PO_4^{3-} increased to 10 mM, the removal efficiency of As(III) and As(V) remained only 31.26% and 1.42%, respectively. The reason could be that PO_4^{3-} had stronger affinity towards iron(oxy)hydroxides than arsenic, and it can form inner-sphere surface complexes with hydroxyl groups more easily, resulting in low removal efficiency of arsenic[44, 45].

3.5. Removal mechanism

The removal mechanisms of As(III) and As(V) exist differences due to their various species in water. Herein, the mechanism could be explained under the following aspects:

3.5.1. pH

Fig. 6 depicts the effect of pH on arsenic adsorption by $FeMnO_x$/RGO. The removal efficiency of As(V) was comparatively higher than As(III) in the pH range 3-9 with 1 mg L^{-1} initial arsenic concentration, which confirmed that As(V) was easier and more efficient to be removed from aqueous system using $FeMnO_x$/RGO. The trend of removal efficiency of As(V) dropped much slightly at pH range 3-9, whereas rapid decline emerged in the pH range 9-11. This phenomenon could be explained by the point of zero charge (pH_{PZC}) of the sorbent. In this study, the pH_{PZC} value of $FeMnO_x$/RGO was calculated to be 6.56, which was shown in the inset of Fig. 6. Detailed information about pH_{PZC} can be obtained in Figure S4. As(V) is usually present in the form of anionic species in aqueous solutions, such as $H_2AsO_4^-$, $HAsO_4^{2-}$ [14, 46]. Thus, when pH < pH_{PZC}, the surface of adsorbent was positively charged,

resulting in more adsorption sites for anionic arsenate because of stronger electrostatic attraction. At pH > pH_{PZC}, the removal efficiency of As(V) began to decrease, and especially when pH > 9, the adsorbent possessed highly negative surface charge and exhibited stronger electrostatic repulsion towards As(V), causing much lower removal efficiency of As(V). Similar explanations were also obtained by Chandra et al.[38].

As presented in Fig. 6, the removal efficiency of As(III) maintained over 80% in the pH between 3 and 9 and it dropped when pH > 9, indicating that part of neutral As(III) was converted into anionic As(V), which brought out electrostatic repulsion between negatively charged sorbent's surface and anionic As(V), together with the competition for active adsorption sites by OH^-.

Variations of pH values before and after arsenic removal were investigated and presented in Table S2. It can be seen that in acidic environment, pH slightly increased after arsenic adsorption, whereas the pH decreased under alkaline conditions demonstrating the possible release of H^+ from the surface of sorbent[39]. There were minor variations between pH values before and after arsenic removal as the initial pH value was around 7, showing the material was stable in real water treatment and it was considered to be a promising adsorbent for arsenic removal. Our results were in agreement with the study reported by Feng et al.[47].

3.5.2. The role of iron and manganese oxides

XPS was used to analyze the valence states of iron and manganese in $FeMnO_x$/RGO with different molar ratios of iron to manganese, as shown in Fig. 7.

385 The peaks $Fe2p_{1/2}$ and $Fe2p_{3/2}$ were located at 724.0 and 710.4 eV, corresponding to
386 Fe(III)[48], and the electron binding energies at 653.3 and 642.0 eV were characteristic
387 of Mn(IV)[12]. No significant changes appeared in Fe2p and Mn2p spectrums with the
388 variations of molar ratios of Fe to Mn, indicating that Fe(III) and Mn(IV) were quite
389 stable in the adsorbent composite.

390 Fig. 8 presents the influence of various molar ratios of iron to manganese in
391 As(III) and As(V) adsorption. In Fig. 8a, when the proportion of MnO_2 increased, the
392 adsorption ability of the sorbent for As(III) removal also enhanced, indicating the
393 oxidation ability of MnO_2. However, too much amount of MnO_2 (nFe:nMn=3:4)
394 resulted in a dramatic decline in the adsorption capacity for As(III), which might be
395 the reason that MnO_2 occupied too many adsorption sites, inhibiting As(III)
396 adsorption. There was a little difference in the removal efficiency of As(V) as
397 nFe:nMn=3:0.5, 3:2 and 3:4. While $FeMnO_x$/RGO (nFe:nMn=3:1) held the highest
398 adsorption capacity among the other adsorbents (Fig. 8b). The results demonstrated
399 that MnO_2 had subtle effect on As(V) adsorption and 3:1 was an appropriate
400 proportion of iron to manganese for arsenic removal. In contrast, when changing the
401 amount of iron oxide, the difference of adsorption capacity for As(V) was more
402 obvious (Fig. 8d) as compared to As(III) (Fig. 8c), which revealed that iron(III) oxide
403 owned the dominant availability for As(V) removal.

404 To understand the role of iron and manganese oxides more clearly, Fig. 9
405 compares the adsorption ability of FeO_x/RGO and MnO_x/RGO with $FeMnO_x$/RGO

406 for As(III) and As(V) adsorption. From Fig. 9, the adsorption capacity of adsorbents
407 for both As(III) and As(V) was in the following order: $FeMnO_x$/RGO > FeO_x/RGO >
408 MnO_x/ RGO. It was obvious that MnO_2 had quite lower adsorption ability for As(III)
409 and As(V); however, MnO_2 was found highly effective for As(III) oxidation. It can be
410 seen in Fig. 10 that after reaction with As(III) solution, MnO_x/RGO showed a peak at
411 48.5 eV, corresponding to As(V), while the peak in XPS spectra of FeO_x/RGO was
412 also the characteristic peak of As(III) (44.3 eV)[31, 49]. Thus, MnO_2 could transform
413 As(III) into As(V) easily during the adsorption process and FeO_x/RGO had higher
414 adsorption capacity for As(V) rather than As(III) (Fig. 9), confirming iron(III) oxide
415 played a key role on As(V) removal.

416 Data fitted by Langmuir model showed that the sum of adsorption capacities of
417 FeO_x/RGO and MnO_x/RGO for As(III) removal was lower than the maximum
418 adsorption amount of As(III) by $FeMnO_x$/RGO (5.96 mg/g + 2.95 mg/g = 8.91 mg/g <
419 22.42 mg/g). Moreover, the results of As(V) (12.14 mg/g + 3.41 mg/g = 15.55 mg/g <
420 22.22 mg/g) were in agreement with that of As(III) (Table S3), confirming that Fe-Mn
421 binary oxide possessed synergistic effects for As(III) and As(V) removal. Thus,
422 combination of both iron oxide and manganese oxide on graphene was very effective
423 and beneficial for arsenic removal.

424 To summarize the possible mechanism of As(III) adsorption on $FeMnO_x$/RGO,
425 the schematic diagram of removal mechanism is shown in Fig. 11. As the adsorbent
426 was added into As(III) solution, the part of As(III) was converted into As(V) by MnO_2.

The reaction pathway involved two steps containing the reduction of Mn(IV) to Mn(III) and then Mn(III) to Mn(II)[31]:

$$MnO_2 + H_3AsO_3 + 2H^+ = Mn^{2+} + H_3AsO_4 + H_2O \quad (5)$$

$$2MnO_2 + H_3AsO_3 = 2MnOOH* + H_3AsO_4 \quad (6)$$

$$2MnOOH* + H_3AsO_3 + 4H^+ = 2Mn^{2+} + H_3AsO_4 + 3H_2O \quad (7)$$

Furthermore, As(V) would diffuse into the aqueous solution because of higher concentration on the surface of MnO_2[23]. Then As(V) together with the minority of As(III) was more attractive to iron(III) oxide attached tightly on graphene. As a consequence, hydroxyl groups on the surface of iron oxide could be replaced by As(III)/As(V) via ligand exchange, forming the inner-sphere surface complexes[50, 51]. Thus, arsenic was eventually adsorbed on $FeMnO_x$/RGO.

3.6. Regeneration and reusability

Relevant experiments about the reusability of this adsorbent were performed. Fig. 12 reveals arsenic removal efficiency on regenerated Fe-Mn/RGO at initial concentration 100 μg L^{-1}. In the five treatment cycles, the majority of As(III) or As(V) was removed and As(III) removal efficiency was always higher than 90%, indicating that the residual concentration of As(III) was still under the standard concentration 10 ppb after the fifth adsorption. These results also indirectly demonstrated that the adsorbed arsenic could be successfully desorbed from Fe-Mn/RGO using 0.1 M NaOH + 0.1 M NaClO as the regenerant. Therefore, this adsorbent possesses good regeneration potential and it will be effectively and consecutively applied in real

448 treatment of arsenic-contaminated water in future.

449 ## 4. Conclusions

450 In summary, $FeMnO_x$/RGO has been successfully prepared and employed for
451 As(III) and As(V) removal from aqueous solutions. Due to huge specific surface area
452 of graphene, Fe-Mn binary oxide was finely dispersed onto the surface of RGO,
453 providing a large number of adsorption active sites for arsenic removal. Results
454 demonstrated that MnO_2 possessed excellent oxidative ability for As(III), while
455 iron(III) oxide was quite efficient to As(V) removal. High removal efficiency by
456 $FeMnO_x$/RGO confirmed that this material could be promising in large scale
457 applications.

458 ## Acknowledgments

459 The authors acknowledge for the financial support of the National Natural
460 Science Foundation of China (No. 21477108, 21277119).

461

References

1. D. Mohan and C.U. Pittman, *J. Hazard. Mater.*, 2007, **142**, 1-53.
2. V.M. Boddu, K. Abburi, J.L. Talbott, E.D. Smith and R. Haasch, *Water Res.*, 2008, **42** , 633-642.
3. WHO, Guidelines for Drinking Water Quality, fourth ed., Geneva, Switzerland, 2011.
4. USEPA, Arsenic Treatment Technology Evaluation Handbook for Small System, EPA 816-R-03-014, Washington, D.C., 2000.
5. C.K. Jain and I. Ali, *Water Res.*, 2000, **34**, 4304-4312.
6. P.L. Smedley and D.G. Kinniburgh, *Appl. Geochem.*, 2002, **17**, 517-568.
7. K. Zhang, V. Dwivedi, C.Y. Chi and J.S. Wu, *J. Hazard. Mater.*, 2010, **182**, 162-168.
8. T.A. Saleh, S. Agarwal and V.K. Gupta, *Appl. Catal. B: Environ.*, 2011, **106**, 46-53.
9. D. Ranjan, M. Talat and S.H. Hasan, *J. Hazard. Mater.*, 2009, **166**, 1050-1059.
10. M. Jang, S.H. Min, T.H. Kim and J.K. Park, *Environ. Sci. Technol.*, 2006, **40**, 1636-1643.
11. K. Banerjee, G.L. Amy, M. Prevost, S. Nour, M. Jekel, P.M. Gallagher and C.D. Blumenschein, *Water Res.*, 2008, **42**, 3371-3378.
12. G.S. Zhang, J.H. Qu, H.J. Liu, R.P. Liu and R.C. Wu, *Water Res.*, 2007, **41**, 1921-1928.

13. P. Mondal, C. Balomajumder and B. Mohanty, *J. Hazard. Mater.*, 2007, **144**, 420-426.

14. T.F. Lin and J.K. Wu, *Water Res.*, 2001, **35**, 2049-2057.

15. R.J. Gohari, W.J. Lau, T. Matsuura and A.F. Ismail, *Sep. Purif. Technol.*, 2013, **118**, 64-72.

16. G.S. Zhang, H.J. Liu, R.P. Liu and J.H. Qu, *J. Hazard. Mater.*, 2009, **168**, 820-825.

17. P. Tamilarasan and S. Ramaprabhu, *AIP Conf. Proc.*, 2012, **1447**, 321-322.

18. Z.G. Liu, F.S. Zhang and R. Sasai, *Chem. Eng. J.*, 2010, **160**, 57-62.

19. X.B. Luo, C.C. Wang, S.L. Luo, R.Z. Dong, X.M. Tu and G.S. Zeng, *Chem. Eng. J.*, 2012, **187**, 45-52.

20. Y. Tian, M. Wu, X.B. Lin, P. Huang and Y. Huang, *J. Hazard. Mater.*, 2011, **193**, 10-16.

21. Y.W. Zhu, S. Murali, W.W. Cai, X.S. Li, J.W. Suk, J.R. Potts and R.S. Ruoff, *Adv. Mater.*, 2010, **22**, 3906-3924.

22. X.S. Lv, X.Q. Xue, G.M. Jiang, D.L. Wu, T.T. Sheng, H.Y. Zhou and X.H. Xu, *J. Colloid Interf. Sci.*, 2014, **417**, 51-59.

23. J. Zhu, S.A. Baig, T.T. Sheng, Z.M. Lou, Z.X. Wang and X.H. Xu, *J Hazard. Mater.*, 2015, **286**, 220-228.

24. W.S. Hummers and R.E. Offeman, *J. Am. Chem. Soc.*, 1958, **80**, 1339

25. X.L. Wu, L. Wang, C.L. Chen, A.W. Xu and X.K. Wang, *J. Mater. Chem.*, 2011,

504 **21**, 17353.

505 26. A. Yürüm, Z.Ö. Kocabaş-Atakl1, M. Sezen, R. Semiat and Y. Yürüm, *Chem.*

506 *Eng. J.*,2014, **242**, 321-332.

507 27. S.W. Liu, S.H. Kang, G.Z. Wang, H.J. Zhao and W.P. Cai, *J. Colloid Interf. Sci.*,

508 2015. DOI: http://dx.doi.org/10.1016/j.jcis.2015.07.038.

509 28. G. Srinivas, Y.W. Zhu, R. Piner, N. Skipper, M. Ellerby and R. Ruoff, *Carbon*,

510 2010, **48**, 630-635.

511 29. Z.S. Wu, W.C. Ren, L. Wen, L.B. Gao, J.P. Zhao, Z.P. Chen, G.M. Zhou, F. Li

512 and H.M. Cheng, *ACS Nano,*2010, **4**, 3187-3194.

513 30. C.B. Wang, J.W. Zhou, J. Ni, Y.L. Cheng and H. Li, *Chem. Eng. J.*, 2014, **253**,

514 130-137.

515 31. G.S. Zhang, J.H. Qu, H.J. Liu, R.P. Liu and G.T. Li, *Environ. Sci. Technol.*, 2007,

516 **41**, 4613-4619.

517 32. Y. Zhang, M. Yang, X.M. Dou, H. He and D.S. Wang, *Environ. Sci. Technol.*,

518 2005, **39**, 7246-7253.

519 33. I. Langmuir, *J. Am. Chem. Soc.*, 1918, **40**, 1361-1403.

520 34. H. Freundlich, *Z. Phys. Chem.*, 1906, **57**, 385-470.

521 35. K. Fytianos, E. Voudrias and E. Kokkalis, *Chemosphere*, 2000, **40**,3-6.

522 36. Z.M. Gu and B.L. Deng, *Environ. Eng. Sci.*, 2007, **24**, 113-121.

523 37. X.J. Guo and F.H. Chen, *Environ. Sci. Technol.*, 2005, **39**, 6808-6818.

524 38. V. Chandra, J. Park, Y. Chun, J.W. Lee, I. Hwang and K.S. Kim, *ACS Nano*, 2010,

4, 3979-3986.

39. S.A. Baig, J. Zhu, N. Muhammad, T.T. Sheng and X.H. Xu, *Biomass Bioenerg*, 2014,**71**, 299-310.

40. S. Lagergren, *Handlingar*, 1898, **24**, 1-39.

41. Y.S. Ho and G. McKay, *Adsorpt. Sci. Technol.*, 1998, **16**, 243-255.

42. L.S. Tan, J. Xu, X.Q. Xue, Z.M. Lou, J. Zhu, S.A. Baig and X.H. Xu, *RSC Advances*, 2014, **4**, 45920-45929.

43. L.J. Dong, P.V. Zinin, J.P. Cowen and L.C. Ming, *J. Hazard. Mater.*, 2009, **168**, 626-632.

44. J.C. Hsu, C.J. Lin, C.H. Liao and S.T. Chen, *Chemosphere*, 2008, **72**, 1049-1055.

45. X.G. Meng, G.P. Korfiatis, S. Bang and K.W. Bang, *Toxicol. Lett.*, 2002, **133**, 103-111.

46. E. Lombi, W.W. Wenzel and R.S. Sletten, *J. Plant Nutr. Soil Sci.*, 1999, **162**, 451-456.

47. L.Y. Feng, M.H. Cao, X.Y. Ma, Y.S. Zhu and C.W. Hu, *J. Hazard. Mater.*, 2012, **217-218**, 439-446.

48. J. Lu, X.L. Jiao, D.R. Chen and W. Li, *J. Phys.Chem. C*, 2009, **113**, 4012-4017.

49. C. Wang, H.J. Luo, Z.L. Zhang, Y. Wu, J. Zhang and S.W. Chen, *J. Hazard. Mater.*, 2014, **268**, 124-131.

50. R.L. Vaughan and B.E. Reed, *Water Res.*, 2005, **39**, 1005-1014.

51. X.J. Guo, Y.H. Du, F.H. Chen, H.S. Park and Y.N. Xie, *J. Colloid Interf. Sci.*,

546 2007, **314**, 427-433.

547

548 # Captions

549 **Table 1.** Langmuir and Freundlich isotherm parameters for As(III) and As(V)
550 adsorption by different mass ratios of Fe-Mn binary oxide to $FeMnO_x$/RGO
551 nanocomposites.

552 **Table 2.** The arsenic adsorption capacity of RGO, bare $FeMnO_x$ and $FeMnO_x$/RGO.
553 The equilibrium adsorption capacity (q_e) was measured in As(III)/As(V)
554 solution of 7 mg L^{-1}.

555 **Table 3.** Comparison of arsenic adsorption capacity with some adsorbent materials in
556 references.

557 **Table 4.** Pseudo-first-order and pseudo-second-order rate constants for As(III) and
558 As(V) adsorption on $FeMnO_x$/RGO.

559

560

561 **Fig. 1.** TEM images of (a) RGO, (b) $FeMnO_x$, (c) $FeMnO_x$/RGO 14%*, (d)
562 $FeMnO_x$/RGO 45%* and (e) $FeMnO_x$/RGO 76.5%*.
563 *: mass ratios of Fe-Mn binary oxide to $FeMnO_x$/RGO nanocomposites.

564 **Fig. 2.** FTIR spectrums of RGO, $FeMnO_x$ and $FeMnO_x$/RGO.

565 **Fig.3.** Effect of different mass ratios of Fe-Mn binary oxide to $FeMnO_x$/RGO
566 nanocomposites for (a) As(III) and (b) As(V) adsorption. Reaction conditions:
567 initial As concentration: 0.2-7.0 mg L^{-1}, adsorbent dose: 0.2 g L^{-1}, contact
568 time: 24 h, solution pH: 7.0 ± 0.1, temperature: 25 ^{o}C.

569 **Fig. 4.** Effect of contact time on (a) As (III) and (b) As (V) removal by $FeMnO_x$/RGO.
570 Reaction conditions: initial As concentration: 1 mg L^{-1}, adsorbent dose: 0.2 g
571 L^{-1}, contact time: 5 min to 24 h, solution pH: 7.0 ± 0.1, temperature: 25 ^oC.

572 **Fig. 5.** Effect of competing ions on (a) As (III) and (b) As (V) removal by
573 $FeMnO_x$/RGO. Reaction conditions: initial As concentration: 1 mg L^{-1},
574 adsorbent dose: 0.2 g L^{-1}, contact time: 24 h, solution pH: 7.0 ± 0.1,
575 temperature: 25 ^oC.

576 **Fig. 6.** Effect of initial pH on As(III) and As(V) removal by $FeMnO_x$/RGO. Reaction
577 conditions: initial As concentration: 1 mg L^{-1}, adsorbent dose: 0.2 g L^{-1},
578 contact time: 24 h, solution pH: 3-11, temperature: 25 ^oC. Inset: the change
579 of zeta potential as a function of pH value.

580 **Fig.** 7**.** XPS spectra of (a) Fe2p and (b) Mn2p: (1) nFe:nMn=0.5:1, (2) nFe:nMn=1:1,
581 (3) nFe:nMn=3:0.5, (4) nFe:nMn=3:1, (5) nFe:nMn=3:2, (6) nFe:nMn=3:4,
582 (7) nFe:nMn=4:1.

583 **Fig. 8.** Effect of different molar ratios of iron to manganese for arsenic adsorption
584 onto $FeMnO_x$/RGO. Reaction conditions: initial As concentration: 0.2-7.0
585 mg L^{-1}, adsorbent dose: 0.2 g L^{-1}, contact time: 24 h, solution pH: 7.0 ± 0.1,
586 temperature: 25 ^oC.

587 **Fig. 9.** The adsorption capacities of $FeMnO_x$/RGO, FeO_x/RGO and MnO_x/RGO for (a)
588 As(III) and (b) As(V) adsorption. Reaction conditions: initial As
589 concentration: 0.2-7.0 mg L^{-1}, adsorbent dose: 0.2 g L^{-1}, contact time: 24 h,

590 solution pH: 7.0 ± 0.1, temperature: 25 ^{o}C.

591 **Fig. 10.** As 3d core levels of $FeMnO_x$/RGO, FeO_x/RGO and MnO_x/RGO after

592 reaction with As(III).

593 **Fig. 11.** Schematic removal mechanism of As(III) on $FeMnO_x$/RGO.

594 **Fig. 12.** Five consecutive adsorption-regeneration cycles on Fe-Mn/RGO for As(III)

595 and As(V) removal.

596

597 **Table 1.** Langmuir and Freundlich isotherm parameters for As(III) and As(V)
598 adsorption by different mass ratios of Fe-Mn binary oxide to $FeMnO_x$/RGO
599 nanocomposites.

Mass ratios of $FeMnO_x$	*Arsenic*	*Langmuir model*			*Freundlich model*		
		b(L/mg)	q_m(mg/g)	R^2	n	K_F(mg/g)·(1/mg)$^{1/n}$	R^2
14%	As(III)	2.50	6.01	0.9824	3.18	3.48	0.9848
	As(V)	2.81	6.44	0.9900	3.16	3.81	0.9861
45%	As(III)	3.46	22.42	0.9827	2.27	14.42	0.9963
	As(V)	17.31	22.22	0.9928	5.34	20.50	0.8955
76.5%	As(III)	77.5	32.26	0.9846	3.62	44.05	0.9947
	As(V)	15.38	22.42	0.9670	5.91	19.59	0.9119

600
601

602 **Table 2.** The arsenic adsorption capacity of RGO, bare $FeMnO_x$ and $FeMnO_x$/RGO.

603 The equilibrium adsorption capacity (q_e) was measured in As(III)/As(V)

604 solution of 7 mg L^{-1}.

Adsobent	*mass ratios of $FeMnO_x$*	*Arsenic*	*q_e*
RGO	0%	As(III)	0.003 (mg As g^{-1})
		As(V)	0.001 (mg As g^{-1})
Bare $FeMnO_x$	100%	As(III)	33.59 (mg As g^{-1} $FeMnO_x$)
		As(V)	23.97 (mg As g^{-1} $FeMnO_x$)
$FeMnO_x$/RGO	14%	As(III)	40.19 (mg As g^{-1} $FeMnO_x$)
		As(V)	44.16 (mg As g^{-1} $FeMnO_x$)
$FeMnO_x$/RGO	45%	As(III)	47.05 (mg As g^{-1} $FeMnO_x$)
		As(V)	49.01 (mg As g^{-1} $FeMnO_x$)
$FeMnO_x$/RGO	76.5%	As(III)	42.12 (mg As g^{-1} $FeMnO_x$)
		As(V)	30.31 (mg As g^{-1} $FeMnO_x$)

605

606 **Table 3.** Comparison of arsenic adsorption capacity with some adsorbent materials in

607 references.

Adsorbent	*Adsorbent dose (g L^{-1})*	*Initial concentration (mg L^{-1})*	*Adsorption capacity (mg g^{-1})*		*Ref.*
			As(III)	*As(V)*	
$FeMnO_x$/RGO	0.2	7	22.17	22.05	This paper
Fe_3O_4-RGO-MnO_2 (3:8)	0.5	10	14.04	12.22	19
Magnetic wheat straw	0.5	28	3.898	8.062	20
HBC-Fe_3O_4-MnO_2 (3:2)	0.2	0.8	2.42	1.45	23
Fe coated mesoporous carbon	3.0	24	5.96	5.15	36
Bead cellulose loaded with iron oxyhydroxide	1.9	7.5	4.09	4.55	37
Magnetite2-RGO	0.2	7	13.10	5.83	38
Magnetic biochar	0.2	0.8	2.0	3.1	39

608

609 **Table 4.** Pseudo-first-order and pseudo-second-order rate constants for As(III) and

610 As(V) adsorption on $FeMnO_x$/RGO.

Arsenic	Pseudo-first-order kinetic model			Pseudo-second-order kinetic model			Experimental data
	k_1(/min)	q_e(mg/g)	R^2	k_2(g/(mg·min))	q_e(mg/g)	R^2	q_e(mg/g)
As(III)	0.0035	2.04	0.9112	7.53e-3	4.59	0.9989	4.57
As(V)	0.0095	2.17	0.9742	1.52e-2	5.24	0.9999	5.18

611

612

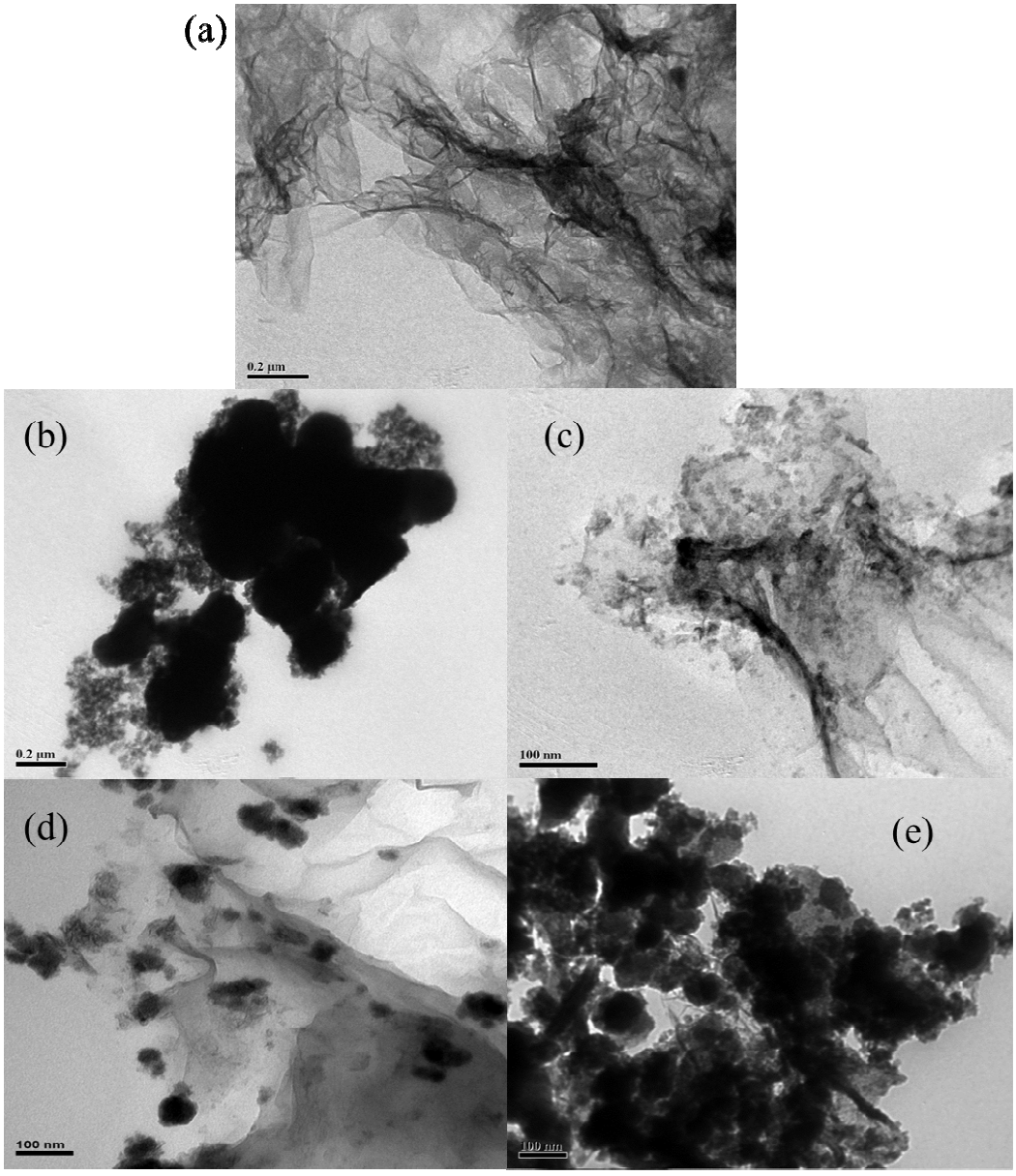

Fig. 1. TEM images of (a) RGO, (b) $FeMnO_x$, (c) $FeMnO_x$/RGO 14%*, (d) $FeMnO_x$/RGO 45%* and (e) $FeMnO_x$/RGO 76.5%*.

*: mass ratios of Fe-Mn binary oxide to $FeMnO_x$/RGO nanocomposites.

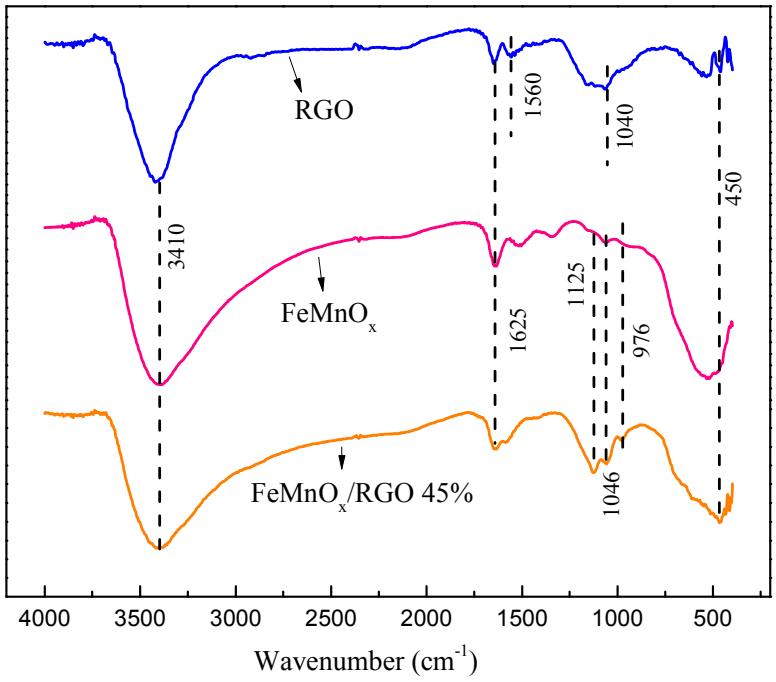

619

620 **Fig. 2.** FTIR spectrums of RGO, $FeMnO_x$ and $FeMnO_x$/RGO.

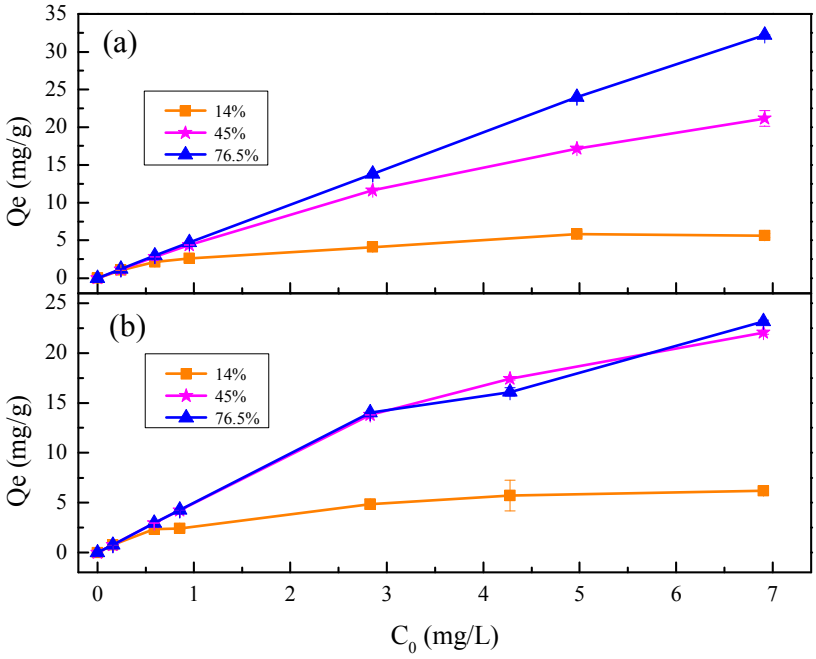

621

622 **Fig.3.** Effect of different mass ratios of Fe-Mn binary oxide to $FeMnO_x$/RGO

623 nanocomposites for (a) As(III) and (b) As(V) adsorption. Reaction conditions:

624 initial As concentration: 0.2-7.0 mg L^{-1}, adsorbent dose: 0.2 g L^{-1}, contact

625 time: 24 h, solution pH: 7.0 ± 0.1, temperature: 25 ^{o}C.

626

627 (a)

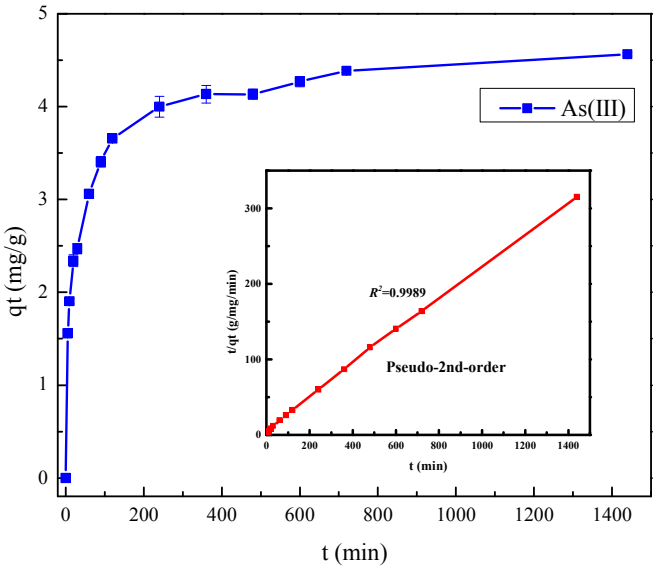

628

629 (b)

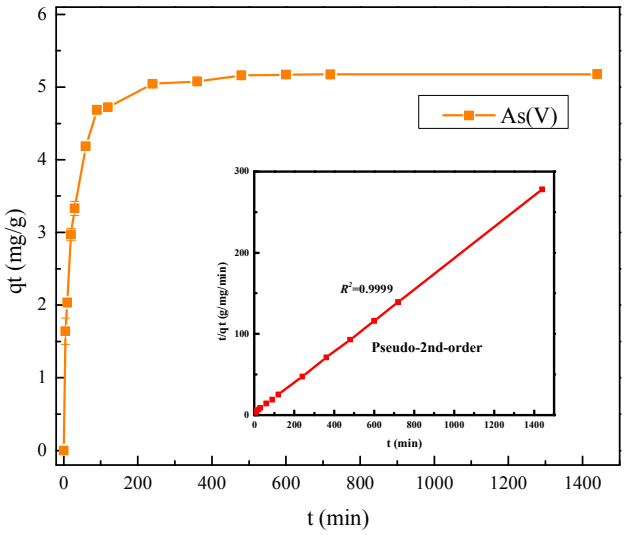

630

631 **Fig. 4.** Effect of contact time on (a) As (III) and (b) As (V) removal by $FeMnO_x$/RGO.

632 Reaction conditions: initial As concentration: 1 mg L^{-1}, adsorbent dose: 0.2 g

633 L^{-1}, contact time: 5 min to 24 h, solution pH: 7.0 ± 0.1, temperature: 25 ^{o}C.

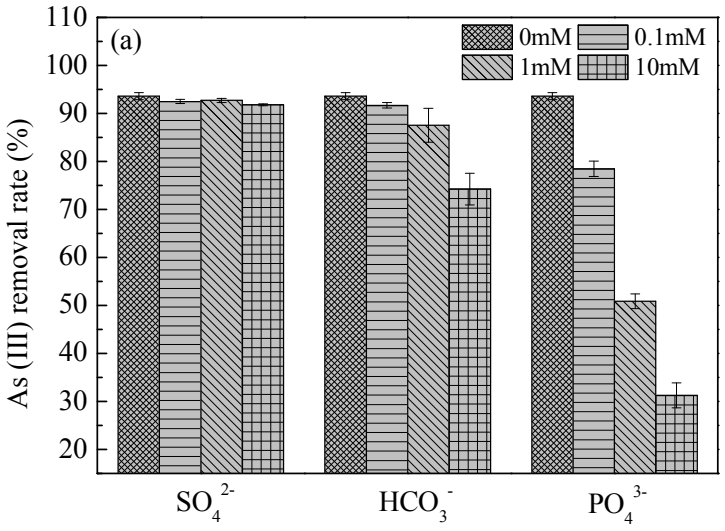

634

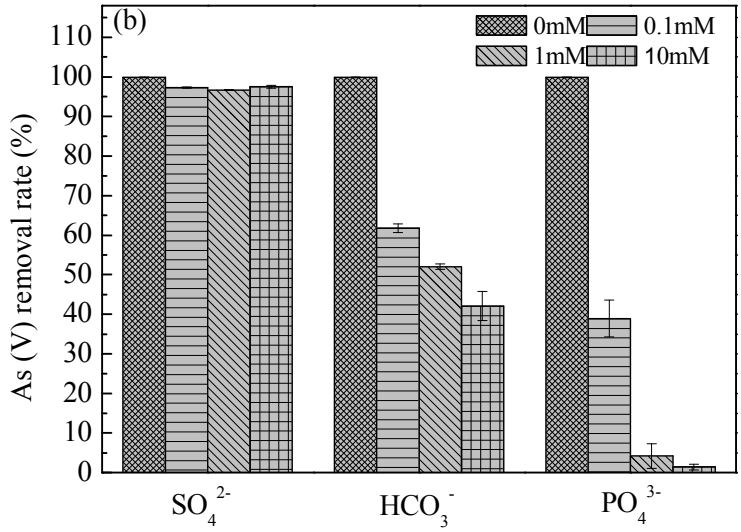

635

636 **Fig. 5.** Effect of competing ions on (a) As (III) and (b) As (V) removal by

637 $FeMnO_x$/RGO. Reaction conditions: initial As concentration: 1 mg L^{-1},

638 adsorbent dose: 0.2 g L^{-1}, contact time: 24 h, solution pH: 7.0 ± 0.1,

639 temperature: 25 ^oC.

640

641

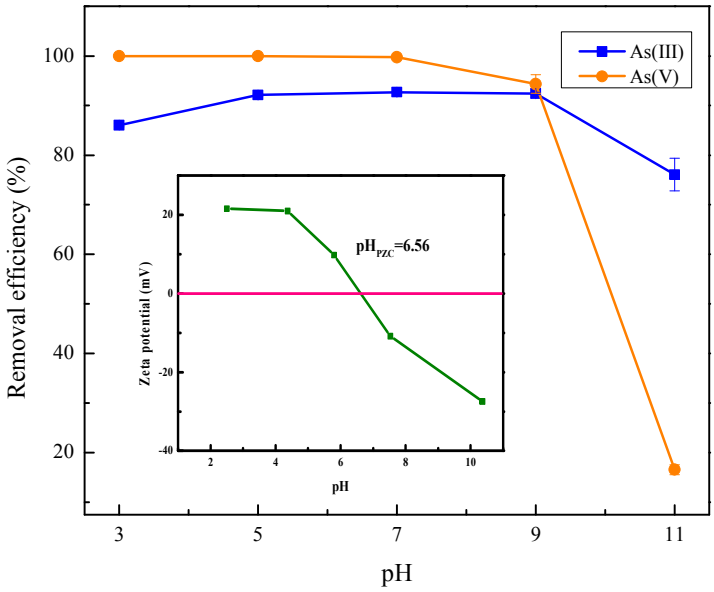

642

643 **Fig. 6.** Effect of initial pH on As(III) and As(V) removal by $FeMnO_x$/RGO. Reaction

644 conditions: initial As concentration: 1 mg L^{-1}, adsorbent dose: 0.2 g L^{-1},

645 contact time: 24 h, solution pH: 3-11, temperature: 25 ^{o}C. Inset: the change

646 of zeta potential as a function of pH value.

647 (a)

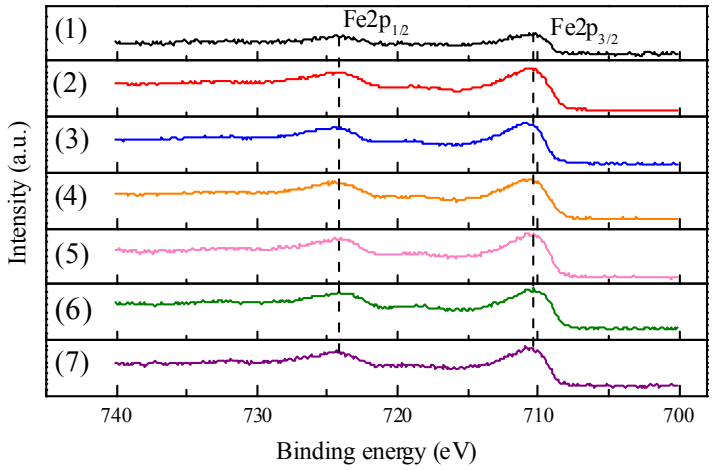

648

649 (b)

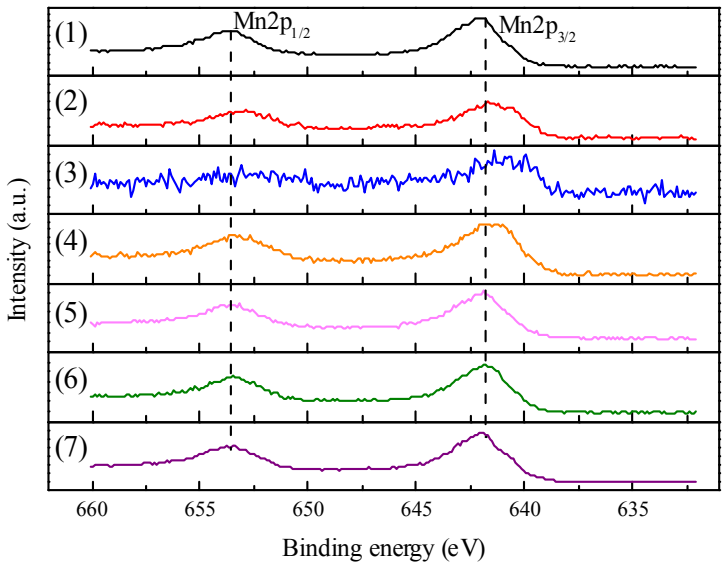

650

651 **Fig.** 7. XPS spectra of (a) Fe2p and (b) Mn2p: (1) nFe:nMn=0.5:1, (2) nFe:nMn=1:1,

652 (3) nFe:nMn=3:0.5, (4) nFe:nMn=3:1, (5) nFe:nMn=3:2, (6) nFe:nMn=3:4,

653 (7) nFe:nMn=4:1.

654

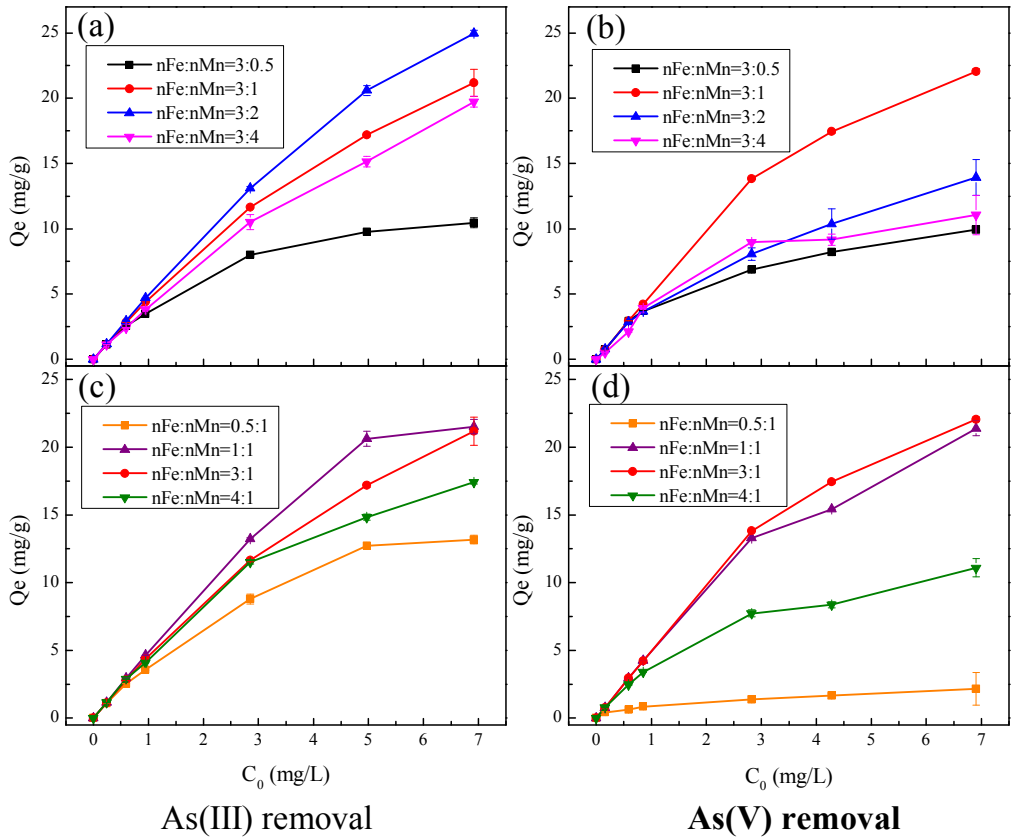

Fig. 8. Effect of different molar ratios of iron to manganese for arsenic adsorption onto $FeMnO_x$/RGO. Reaction conditions: initial As concentration: 0.2-7.0 mg L^{-1}, adsorbent dose: 0.2 g L^{-1}, contact time: 24 h, solution pH: 7.0 ± 0.1, temperature: 25 ^{o}C.

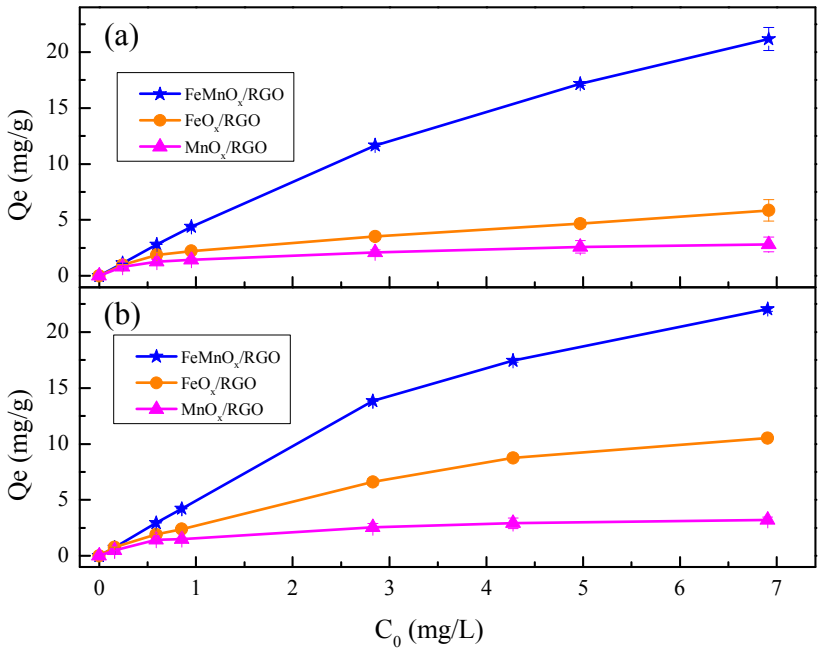

662

663 **Fig. 9.** The adsorption capacities of $FeMnO_x$/RGO, FeO_x/RGO and MnO_x/RGO for (a)

664 As(III) and (b) As(V) adsorption. Reaction conditions: initial As

665 concentration: 0.2-7.0 mg L^{-1}, adsorbent dose: 0.2 g L^{-1}, contact time: 24 h,

666 solution pH: 7.0 ± 0.1, temperature: 25 ^{o}C.

667

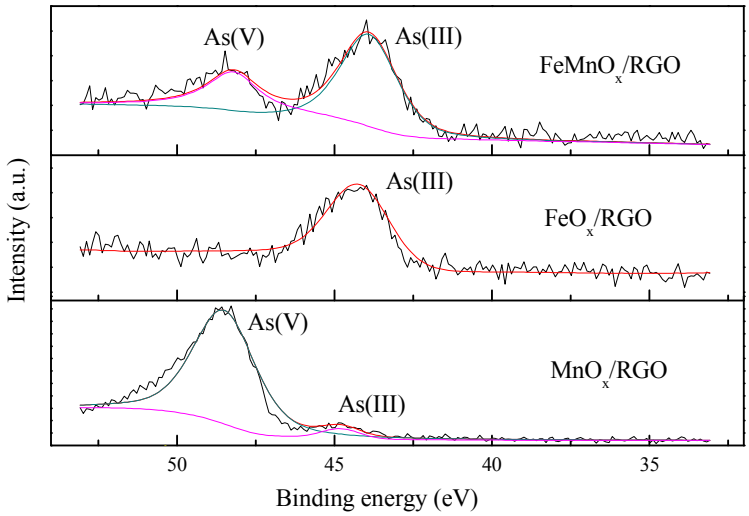

668

669 **Fig. 10.** As 3d core levels of $FeMnO_x$/RGO, FeO_x/RGO and MnO_x/RGO after

670 reaction with As(III).

671

672

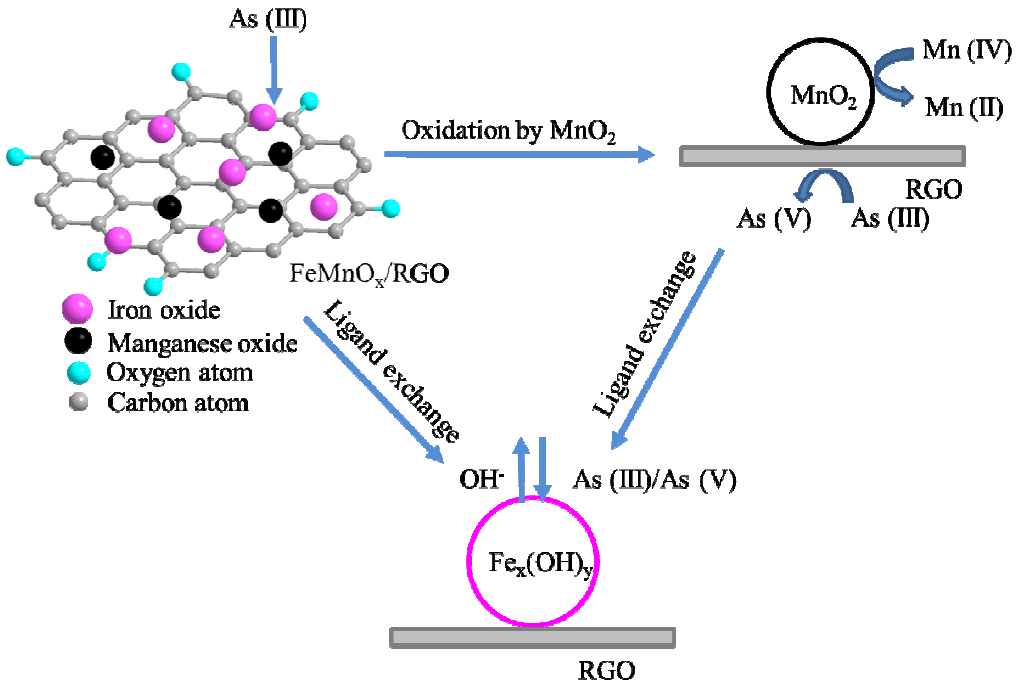

673

674

675 **Fig. 11.** Schematic removal mechanism of As(III) on $FeMnO_x$/RGO.

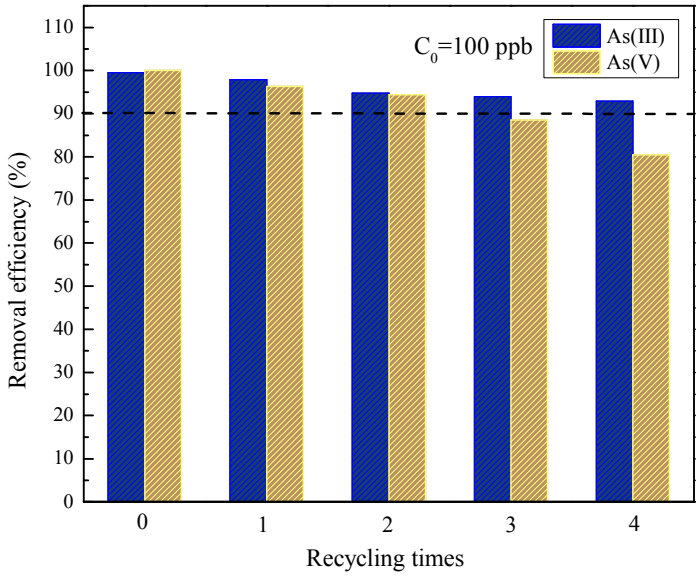

676

677 **Fig. 12.** Five consecutive adsorption-regeneration cycles on Fe-Mn/RGO for As(III)

678 and As(V) removal.

679